

NUMERICAL SIMULATION OF VISCOELASTIC FLOW PAST A CYLINDER

HOWARD H. HU and DANIEL D. JOSEPH

*Department of Aerospace Engineering and Mechanics, University of Minnesota,
110 Union St. SE, Minneapolis, MN 55455 (U.S.A.)*

(Received May 14, 1990)

Abstract

The flow of an upper-convected Maxwell fluid past a circular cylinder is simulated numerically using the algorithm SIMPLER, which is based on a finite volume discretization on a staggered grid of the governing equations and an iterative solution to the nonlinearly coupled equations. The effect of the viscoelasticity of the fluid on the flow is examined. The drag force on the cylinder and the heat transfer from the cylinder to the surrounding fluid are calculated and compared with those obtained in experiments. One feature seen in the experiments is the existence of a critical velocity across which the variation of the drag and heat transfer changes from a characteristic Newtonian variation to a flat response. This feature is interpreted as a change of type when the critical speed U_c of flow becomes greater than the material wave speed $c = \sqrt{\eta/\lambda\rho}$. The numerical computation is completely consistent with this interpretation. Using an Einstein-type formula for the relaxation time $\lambda = A\phi$ with A independent of ϕ we find that the experiments follow a scaling law $U_c\phi^{1/2} = \text{constant}$, where ϕ is the mass fraction of polymers in water in the regime of extreme dilution, the drag reduction range, consistent with the interpretation that $U_c = c$.

Keywords: change of type; dilute polymer solution; relaxation; viscoelastic flow past cylinder; vorticity shock; wave propagation

1. Introduction

It is known that shear waves can propagate in a viscoelastic fluid with instantaneous elasticity. When the flow velocity is larger than the shear wave velocity, the governing vorticity equation undergoes a change of type. It has

been suggested by Joseph and coworkers [1–4] that some interesting viscoelastic phenomena can be associated with this change of type. Some of the examples are sink flow [5], delayed die swell [3] and flow around bodies [4].

For viscoelastic flow around a circular cylinder, James and Acosta [6] reported a critical phenomenon in which the heat transfer from the cylinder to the surrounding fluid becomes essentially independent of the Reynolds number when the Reynolds number is beyond a critical value. James and Gupta [7] observed the same kind of behavior for the drag coefficient. The velocity measurements of Koniuta et al. [8] revealed a stagnant or nearly stagnant region around the cylinder when the velocity was greater than a critical velocity. Ultman and Denn [9] presented an analysis which suggested that the equation for the forward component of velocity changes type when the flow velocity exceeds shear wave speed, and they applied this idea to the experiments of James and Acosta [6]. Actually, the forward velocity does not change type but the vorticity does; see Joseph [4].

Crochet and Delvaux [10,11] analyzed numerically the flow of an upper-convected Maxwell fluid past a circular cylinder. They used a finite element method which was developed for calculating highly viscoelastic flows [12]. The algorithm is characterized by the bilinear subelements for the stresses and the use of streamline-upwinding for discretizing the constitutive equations. They examined the consequences of the transition from sub- to supercritical flow regime upon momentum and heat transfer properties. Their simulation confirms the experimentally observed change from Newtonian-like variations of the transport properties to constant transport properties for velocities exceeding the shear wave speed.

In the present paper, we simulated the flow of an upper convected Maxwell fluid around a cylinder using the algorithm SIMPLER (semi-implicit method for pressure-linked equations revised) which was introduced by Patankar [13] and successfully used in solving problems of heat transfer and fluid flow of Newtonian fluids. We find that with minor modifications in solving the stress equations SIMPLER works well for the viscoelastic flows in this problem and converges for relatively high Weissenberg number. The computed drag force on the cylinder and the heat transfer from the cylinder to the surrounding fluid are compared with those obtained in experiments of James and Acosta [6]. The numerical results display many details of the flow.

2. Basic equations

Consider a two-dimensional uniform flow for a Maxwell fluid past a circular cylinder of diameter d in the plane. We limit ourselves to flows of low and medium Reynolds numbers which are steady, symmetric and

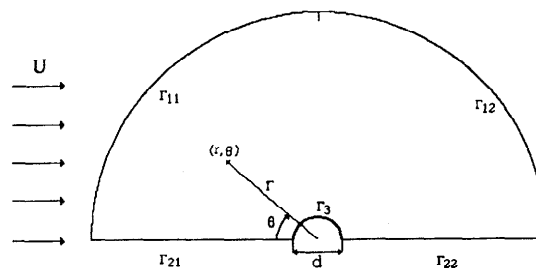


Fig. 1. Flow geometry and boundaries.

without instability. The geometry of the problem is shown in Fig. 1. In the figure, Γ_{11} is the inflow and Γ_{12} is the outflow boundary, Γ_{21} and Γ_{22} are the symmetry boundaries and Γ_3 is the solid boundary on the cylinder surface. The outer boundary Γ_{11} and Γ_{12} is assumed to be far away from the cylinder. In our computation the radius of this outer boundary r_∞ is chosen to be about 50 times the radius of the cylinder.

We need to solve

$$\nabla \cdot \mathbf{u} = 0 \quad (1)$$

and

$$\rho(\mathbf{u} \cdot \nabla) \mathbf{u} = -\nabla p + \mathbf{f} + \nabla \cdot \boldsymbol{\tau}, \quad (2)$$

where ρ is the density of the fluid, \mathbf{u} the velocity, p the pressure, \mathbf{f} the body force which is assumed to be zero in this problem, and $\boldsymbol{\tau}$ the extra stress tensor which is given by the constitutive equation

$$\lambda \overset{\nabla}{\tau} + \boldsymbol{\tau} = 2\eta \mathbf{D} \quad (3)$$

for an upper-convected Maxwell fluid. In the constitutive equation λ is the relaxation time, η the shear viscosity, \mathbf{D} the rate of deformation tensor and $\overset{\nabla}{\tau}$ denotes the upper-convected derivative of $\boldsymbol{\tau}$ defined by

$$\overset{\nabla}{\tau} = \frac{\partial \boldsymbol{\tau}}{\partial t} + (\mathbf{u} \cdot \nabla) \boldsymbol{\tau} - (\nabla \mathbf{u}) \boldsymbol{\tau} - \boldsymbol{\tau} (\nabla \mathbf{u})^T, \quad (4)$$

where $(\nabla \mathbf{u})_{ij} = \partial u_i / \partial x_j$. In the present problem we also wish to evaluate the effect of viscoelasticity upon the heat transfer from the cylinder to the surrounding fluid. We assume that the viscous heating is negligible and that temperature differences in the flow are small and such that the fluid properties (ρ , λ and η) do not change. Then the temperature field is decoupled from the velocity field; the energy equation is simply

$$c_p \rho (\mathbf{u} \cdot \nabla) T = \kappa \Delta T, \quad (5)$$

where T is the temperature, c_p the heat capacity and κ the thermal conductivity.

We shall scale length with the diameter of the cylinder d , velocity with the free stream velocity U , pressure with ρU^2 and stress with $\eta U/d$, and use the same symbol for the dimensional and dimensionless quantities. In the dimensionless form the equations of momentum and the constitutive and the temperature equations are consequently

$$(\mathbf{u} \cdot \nabla) \mathbf{u} = -\nabla p + \frac{1}{\mathcal{R}} \Delta \mathbf{u} + \frac{1}{\mathcal{R}} \nabla \cdot \boldsymbol{\tau}_E, \quad (6)$$

$$W [(\mathbf{u} \cdot \nabla)(\boldsymbol{\tau}_E + \boldsymbol{\tau}_N) - \nabla \mathbf{u}(\boldsymbol{\tau}_E + \boldsymbol{\tau}_N) - (\boldsymbol{\tau}_E + \boldsymbol{\tau}_N) \nabla \mathbf{u}^T] + \boldsymbol{\tau}_E = \mathbf{0}, \quad (7)$$

$$\mathcal{R} Pr (\mathbf{u} \cdot \nabla) T = \Delta T, \quad (8)$$

where for the convenience of numerical treatment the extra stress is split into two parts $\boldsymbol{\tau} = \boldsymbol{\tau}_N + \boldsymbol{\tau}_E$ with $\boldsymbol{\tau}_N = 2\eta \mathbf{D}$ being the pseudo-Newtonian part and $\boldsymbol{\tau}_E$ being the part due to the elasticity, the dimensionless temperature is taken as $(T - T_\infty)/T_\infty$ (T_∞ is the temperature of the coming fluid). In these equations the non-dimensional parameters \mathcal{R} (Reynolds number), W (Weissenberg number) and Pr (Prandtl number) are defined as

$$\mathcal{R} = \rho U d / \eta,$$

$$W = \lambda U / d, \quad (9)$$

$$Pr = c_p \rho / \kappa.$$

It is helpful to introduce another two non-dimensional parameters, the viscoelastic Mach number M and the elasticity number E which are defined by

$$M = \sqrt{W \mathcal{R}} = \mathcal{R} \sqrt{E} = \frac{U}{c},$$

$$E = \frac{W}{\mathcal{R}} = \frac{\eta \lambda}{\rho d^2}, \quad (10)$$

where

$$c = \sqrt{\frac{\eta}{\lambda \rho}} \quad (11)$$

is the speed of shear waves in a Maxwell fluid. In the study of change of type the Mach number M is an essential parameter: $M=1$ characterizes many critical phenomena observed experimentally [4]. The elasticity number E depends only on the fluid properties and the flow geometry. In our computation we choose the pair (\mathcal{R}, E) as the independent parameters, and simulate the flow in experiments by keeping E fixed and adjusting \mathcal{R} .

We use the polar coordinate system shown in Fig. 1, writing the velocity as

$$\mathbf{u} = u_r \mathbf{e}_r + u_\theta \mathbf{e}_\theta$$

and the stress as

$$\boldsymbol{\tau}_E = \tau_{Err} \mathbf{e}_r \mathbf{e}_r + \tau_{E\theta\theta} \mathbf{e}_\theta \mathbf{e}_\theta + \tau_{Er\theta} (\mathbf{e}_r \mathbf{e}_\theta + \mathbf{e}_\theta \mathbf{e}_r).$$

Equations (1), (6), (7) and (8) in component form are

$$\frac{\partial u_r}{\partial r} + \frac{u_r}{r} + \frac{\partial u_\theta}{r \partial \theta} = 0, \quad (12)$$

$$\begin{aligned} u_r \frac{\partial u_r}{\partial r} + u_\theta \frac{\partial u_r}{r \partial \theta} = & -\frac{\partial p}{\partial r} + \frac{1}{\mathcal{R}} \left(\frac{\partial^2 u_r}{\partial r^2} + \frac{\partial u_r}{r \partial r} + \frac{\partial^2 u_r}{r^2 \partial \theta^2} \right) \\ & + \left[\frac{u_\theta^2}{r} - \frac{1}{\mathcal{R}} \left(\frac{u_r}{r^2} + \frac{2}{r^2} \frac{\partial u_\theta}{\partial \theta} \right) + \frac{1}{\mathcal{R}} \left(\frac{\partial \tau_{Err}}{\partial r} + \frac{\partial \tau_{Er\theta}}{r \partial \theta} \right. \right. \\ & \left. \left. + \frac{\tau_{Err} - \tau_{E\theta\theta}}{r} \right) \right], \end{aligned} \quad (13)$$

$$\begin{aligned} u_r \frac{\partial u_\theta}{\partial r} + u_\theta \frac{\partial u_\theta}{r \partial \theta} = & -\frac{\partial p}{r \partial \theta} + \frac{1}{\mathcal{R}} \left(\frac{\partial^2 u_\theta}{\partial r^2} + \frac{\partial u_\theta}{r \partial r} + \frac{\partial^2 u_\theta}{r^2 \partial \theta^2} \right) \\ & + \left[-\frac{u_r u_\theta}{r} - \frac{1}{\mathcal{R}} \left(\frac{u_\theta}{r^2} - \frac{2}{r^2} \frac{\partial u_r}{\partial \theta} \right) + \frac{1}{\mathcal{R}} \left(\frac{\partial \tau_{Er\theta}}{\partial r} + \frac{\partial \tau_{E\theta\theta}}{r \partial \theta} \right. \right. \\ & \left. \left. + 2 \frac{\tau_{Er\theta}}{r} \right) \right], \end{aligned} \quad (14)$$

$$\begin{aligned} W \left(u_r \frac{\partial \tau_{Err}}{\partial r} + u_\theta \frac{\partial \tau_{Err}}{r \partial \theta} \right) = & -\tau_{Err} + 2W \left[\frac{\partial u_r}{\partial r} (\tau_{Err} + \tau_{Nr\theta}) \right. \\ & \left. + \frac{\partial u_r}{r \partial \theta} (\tau_{Er\theta} + \tau_{Nr\theta}) \right] - W \left(u_r \frac{\partial \tau_{Nr\theta}}{\partial r} + u_\theta \frac{\partial \tau_{Nr\theta}}{r \partial \theta} \right), \end{aligned} \quad (15)$$

$$\begin{aligned} W \left(u_r \frac{\partial \tau_{E\theta\theta}}{\partial r} + u_\theta \frac{\partial \tau_{E\theta\theta}}{r \partial \theta} \right) = & -\tau_{E\theta\theta} + 2W \left[\left(\frac{\partial u_\theta}{\partial r} - \frac{u_\theta}{r} \right) (\tau_{Er\theta} + \tau_{Nr\theta}) \right. \\ & \left. - \frac{\partial u_r}{\partial r} (\tau_{E\theta\theta} + \tau_{Nr\theta\theta}) \right] - W \left(u_r \frac{\partial \tau_{Nr\theta\theta}}{\partial r} + u_\theta \frac{\partial \tau_{Nr\theta\theta}}{r \partial \theta} \right), \end{aligned} \quad (16)$$

$$\begin{aligned} W \left(u_r \frac{\partial \tau_{Er\theta}}{\partial r} + u_\theta \frac{\partial \tau_{Er\theta}}{r \partial \theta} \right) = & -\tau_{Er\theta} + W \left[\frac{\partial u_r}{r \partial \theta} (\tau_{E\theta\theta} + \tau_{Nr\theta\theta}) + \left(\frac{\partial u_\theta}{\partial r} - \frac{u_\theta}{r} \right) \right. \\ & \left. \times (\tau_{Err} + \tau_{Nr\theta}) \right] - W \left(u_r \frac{\partial \tau_{Nr\theta}}{\partial r} + u_\theta \frac{\partial \tau_{Nr\theta}}{r \partial \theta} \right), \end{aligned} \quad (17)$$

$$\mathcal{R} Pr \left(u_r \frac{\partial T}{\partial r} + u_\theta \frac{\partial T}{r \partial \theta} \right) = \frac{\partial^2 T}{\partial r^2} + \frac{\partial T}{r \partial r} + \frac{\partial^2 T}{r^2 \partial \theta^2}. \quad (18)$$

Thus we have seven equations for seven unknowns u_r , u_θ , p , τ_{Err} , $\tau_{E\theta\theta}$, $\tau_{Er\theta}$, T . The pseudo-Newtonian part of the extra stress τ_N can be evaluated from the velocities (u_r , u_θ) by the definition

$$\begin{aligned}\tau_{Nrr} &= 2 \frac{\partial u_r}{\partial r}, \\ \tau_{N\theta\theta} &= \frac{\partial u_r}{r \partial \theta} + \frac{\partial u_\theta}{\partial r} - \frac{u_\theta}{r}, \\ \tau_{N\theta r} &= 2 \left(\frac{\partial u_\theta}{r \partial \theta} + \frac{u_r}{r} \right) = -\tau_{Nrr}.\end{aligned}\quad (19)$$

To complete the specification of the problem, we need appropriate boundary conditions. At the inflow boundary Γ_{11} ($r = r_\infty$, $0 \leq \theta \leq \pi/2$) the velocities, the stresses and the temperature are prescribed:

$$\begin{aligned}u_r &= -\cos \theta, \quad u_\theta = \sin \theta, \quad T = 0, \\ \tau_{Err} &= 0, \quad \tau_{Er\theta} = 0, \quad \tau_{E\theta\theta} = 0.\end{aligned}\quad (20)$$

At the symmetry boundaries Γ_{21} and Γ_{22} ($0.5 \leq r \leq r_\infty$, $\theta = 0$ and $\theta = \pi$) they satisfy

$$\begin{aligned}\frac{\partial u_r}{\partial \theta} &= 0, \quad u_\theta = 0, \quad \frac{\partial T}{\partial \theta} = 0, \\ \frac{\partial \tau_{Err}}{\partial \theta} &= 0, \quad \tau_{Er\theta} = 0, \quad \frac{\partial \tau_{E\theta\theta}}{\partial \theta} = 0.\end{aligned}\quad (21)$$

On the solid boundary of the cylinder surface Γ_3 ($r = 0.5$, $0 \leq \theta \leq \pi$), the velocities are zero by the no-slip condition, the temperature is assumed to be constant and fixed, and the stresses are obtained by evaluating eqns. (15)–(17) on the surface of the cylinder:

$$\begin{aligned}u_r &= 0, \quad u_\theta = 0, \quad T = 1, \\ \tau_{Err} &= 0, \quad \tau_{Er\theta} = 0, \quad \tau_{E\theta\theta} = 2W \left(\frac{\partial u_\theta}{\partial r} \right)^2.\end{aligned}\quad (22)$$

Also, at the outflow boundary Γ_{12} ($r = r_\infty$, $\pi/2 < \theta \leq \pi$) we simply assume that the flow is convection dominant and the diffusion for the flow quantities can be neglected; this means that the flow quantities at this boundary are determined by the flow quantities just upstream using streamline-upwinding.

3. Computation of additional quantities

In the computation we solve for the velocities, the pressure and the stresses in each iteration. Since the temperature field does not affect the

velocity, the heat equation (18) is solved after the iteration converges. Some additional quantities are also calculated. We evaluate the stream function ψ and the vorticity ω which are defined by

$$u_r = -\frac{\partial \psi}{r \partial \theta}, \quad u_\theta = \frac{\partial \psi}{\partial r}, \quad (23)$$

$$\omega = \frac{\partial u_\theta}{\partial r} + \frac{u_\theta}{r} - \frac{\partial u_r}{r \partial \theta}. \quad (24)$$

From the computed values of the pressure and the pseudo-Newtonian stresses on the surface of the cylinder it is easy to obtain the drag force acting on the cylinder. The dimensional drag force per unit length on the cylinder is found to be

$$F_x = \rho U^2 d \int_0^\pi \left(p \cos \theta + \frac{1}{\mathcal{R}} \tau_{Nr\theta} \sin \theta \right)_{r=d/2} d\theta, \quad (25)$$

which has two contributions, one from the pressure and the other from the pseudo-Newtonian shear stress. In writing (25) we noted that the contribution to the drag of the elastic part of the extra stress vanishes because $\tau_{Er\theta} = 0$ on the surface of the cylinder. The drag coefficient is given by

$$C_D = \frac{F_x}{(\rho/2)U^2 d}. \quad (26)$$

In our computation of heat transfer, we prescribe the upstream temperature as T_∞ (in dimensionless form $T = 0$), and the temperature on the cylinder surface as $T_0 = 2T_\infty$ (in dimensionless form $T = 1$). The dimensional average heat flux from the cylinder to the surrounding fluid is

$$Q = \frac{1}{\pi} \int_0^\pi \left(\kappa \frac{\partial T}{\partial r} \right)_{r=d/2} d\theta. \quad (27)$$

Thus the Nusselt number which characterizes the heat transfer from the cylinder to the surrounding fluid is defined as

$$Nu = \frac{Qd}{\kappa(T_0 - T_\infty)} = \frac{Qd}{\kappa T_\infty}. \quad (28)$$

4. Numerical method

The coupled equations (12)–(17) and the heat equation (18) are solved with algorithm SIMPLER (semi-implicit method for pressure-linked equations revised) introduced by Patankar [13]. This algorithm was successfully implemented for many problems of Newtonian fluid flow and heat transfer in both laminar and turbulent situations. The algorithm is based on a finite

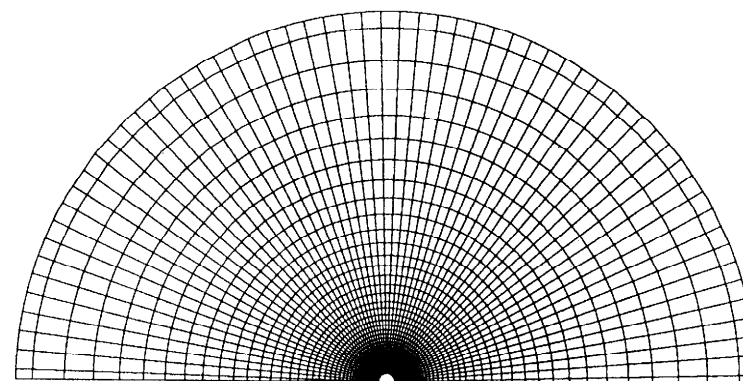
volume discretization on a staggered grid of the governing equations. The solution to the nonlinearly coupled equations is then obtained through an iterative procedure.

Our computation is based on a general program used in the course Computation of Heat Transfer and Fluid Flow (ME8352) given by Professor Patankar at the University of Minnesota. In the program each equation is discretized into a five-point form which relates the variable at the current grid point with its values at the four neighboring points. The discretized equation is solved by first a block correction procedure in two (r and θ) directions and then four sweeps (bottom \rightarrow top \rightarrow bottom and left \rightarrow right \rightarrow left) of line-by-line iteration in which the equation is written as scalar tridiagonal systems along each r grid line (or each θ grid line) and solved directly using the TDMA (tridiagonal matrix algorithm), as described in Patankar [13]. Since there are no second-order diffusion terms in the stress equations (15)–(17), the stress equations are discretized using the upwinding scheme. In the original program three stress components are solved separately one after another. The discretized stress equations can be written in a matrix form

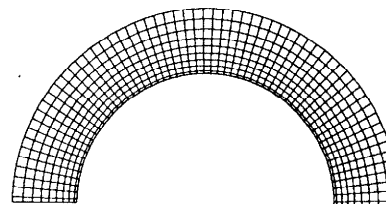
$$\mathbf{M}_p \mathbf{T}_{i,j} = \mathbf{M}_e \mathbf{T}_{i+1,j} + \mathbf{M}_w \mathbf{T}_{i-1,j} + \mathbf{M}_n \mathbf{T}_{i,j+1} + \mathbf{M}_s \mathbf{T}_{i,j-1} + \mathbf{S}, \quad (29)$$

where matrix \mathbf{M}_p is 3×3 and \mathbf{M}_e , \mathbf{M}_w , \mathbf{M}_n and \mathbf{M}_s are 3×3 diagonal, $\mathbf{T} = \{\tau_{rr}, \tau_{\theta\theta}, \tau_{r\theta}\}^T$ and \mathbf{S} are vectors of three components, the subscript (i, j) indicates the value of \mathbf{T} at grid point $\theta = \theta_i$ and $r = r_j$. Based on (29) the scalar form of block correction and line-by-line iteration can be easily modified into a vector form for \mathbf{T} . Thus the three stress components are solved and updated at the same time. In a simpler version, when the matrix \mathbf{M}_p is diagonal, (29) is three scalar equations. The solution of the stress components in this form helps the convergence of the algorithm. In our iterative procedure an underrelaxation parameter α is introduced, which is adjusted according to the elasticity number E and the Reynolds number \mathcal{R} in the problem. For example, when $E = 1$ we used $\alpha = 0.9$ for \mathcal{R} up to 1.5, and $\alpha = 0.1$ for $\mathcal{R} = 7.0$. If α is not appropriate the iteration usually blows up within 50 steps.

The computational domain shown in Fig. 1 is divided into small control volumes. At the center of each control volume lies a grid point. The pressure and the stress components are discretized using their values at these grid points. The velocities u_r and u_θ are discretized using their values at the control volume faces in the r and θ direction respectively. Three meshes are used in the computation with increasingly refined control volumes in the radial direction near the cylinder surface. Figure 2 shows the grid lines used in mesh 2 which are used in most of the computations. There are 60 uniform “control volumes” in the θ direction, and 50 non-uniform “control volumes”



(a)



(b)

Fig. 2. Grid lines used in mesh 2. (a) Overall view. There are 60 uniform control volumes in the θ direction and 50 non-uniform control volumes in the r direction with the smallest of them of size $0.02d$ and a geometric ratio of 1.1. The radius of the outer boundary is $r_\infty = 23.8d$. (b) Close view near the cylinder.

in the r direction with the smallest of them of size $0.02d$ and a geometric ratio of 1.1. The non-dimensional radius of the outer boundary is $r_\infty = 23.8$. Mesh 1 is a coarser version of mesh 2; it simply doubles the size of the control volumes in the radial direction, with 43 control volumes in the r direction. Mesh 3 is a refined version of mesh 2; it reduces the size of the control volumes in the radial direction by a factor of 2, with 58 control volumes in the r direction. The total numbers of grid points used in these three meshes are 2790, 3224 and 3720 respectively.

Figure 3 shows the variation of the three extra stress components and the pressure along path s indicated in the figures (along the symmetry boundaries

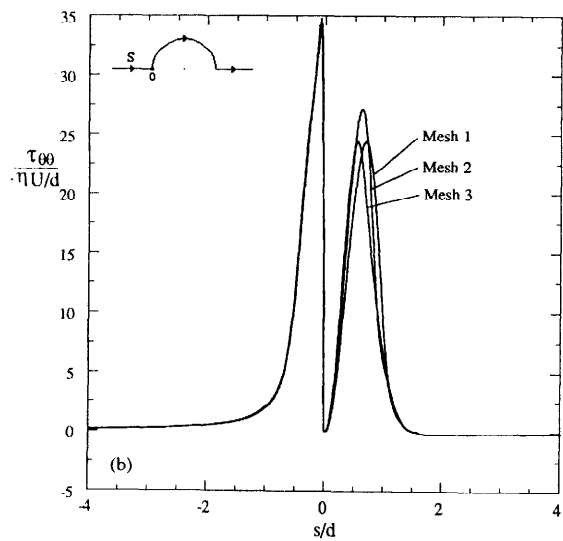
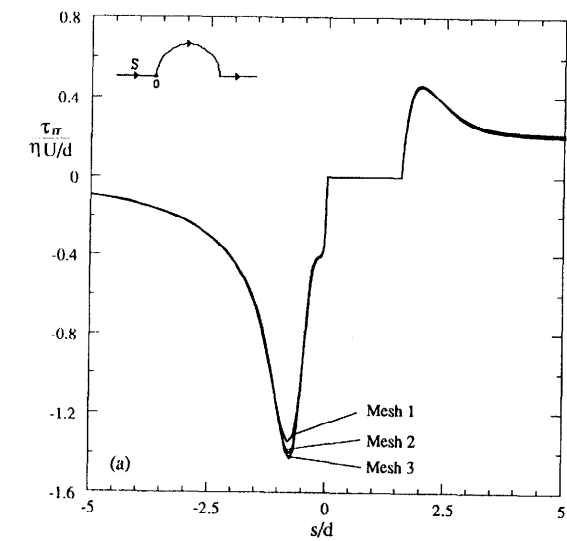


Fig. 3. Variation of the extra stress components (a) τ_{rr} , (b) $\tau_{\theta\theta}$ and (c) $\tau_{r\theta}$ and (d) the pressure p along the path s indicated in the figures, for three meshes with $\mathcal{R} = 4.0$ and $E = 1.0$.

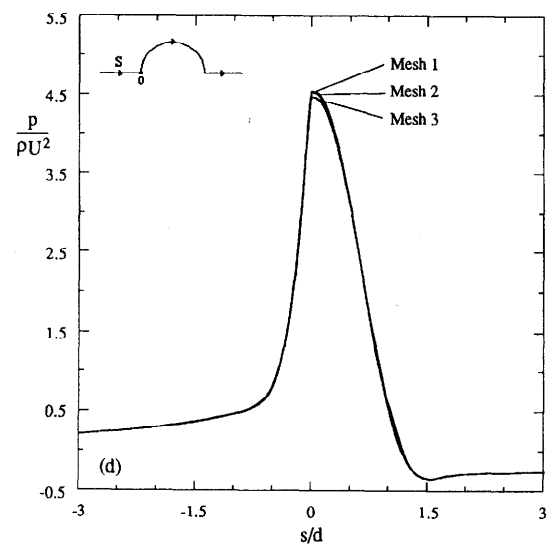
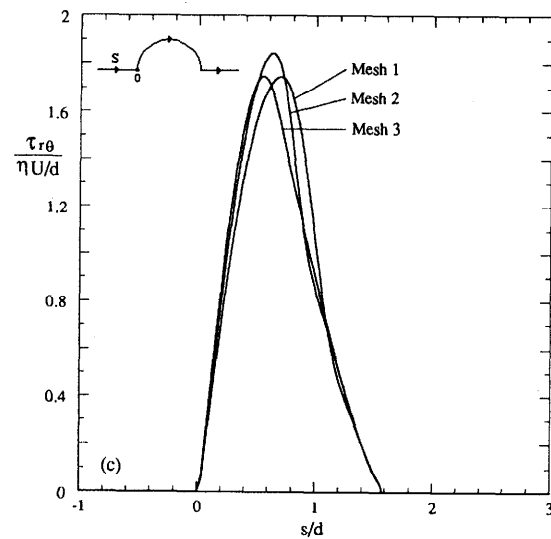


Fig. 3 (continued).

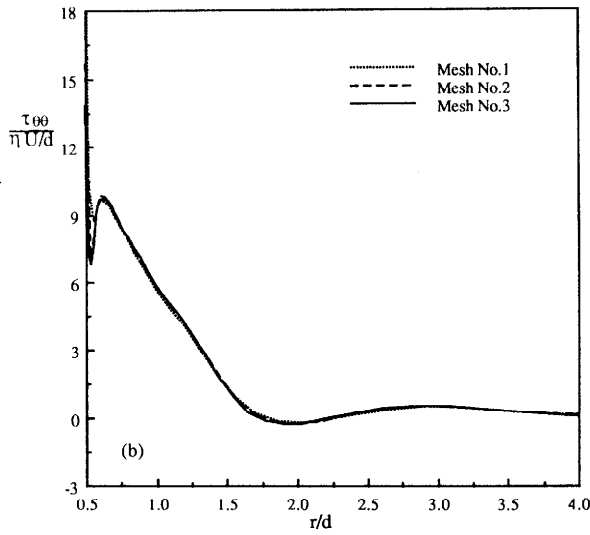
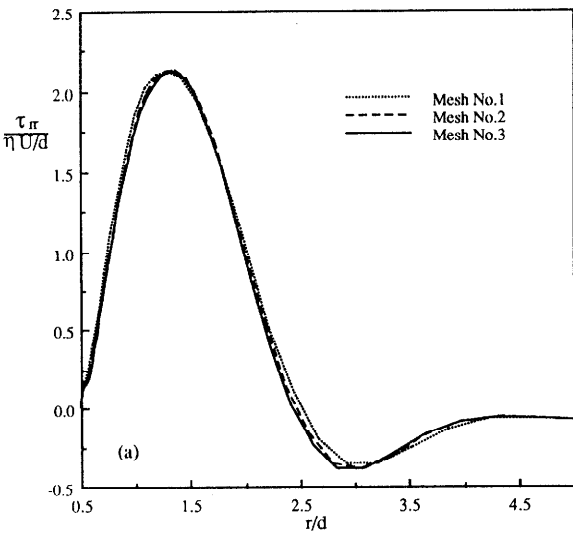


Fig. 4. Extra stress components (a) τ_{rr} , (b) $\tau_{\theta\theta}$ and (c) $\tau_{r\theta}$ along the radial direction just above the cylinder ($\theta = \pi/2$), when $\mathcal{R} = 4$ and $E = 1$ for three meshes. There is a stress boundary layer on the cylinder surface where the stresses $\tau_{\theta\theta}$ and $\tau_{r\theta}$ vary rapidly.

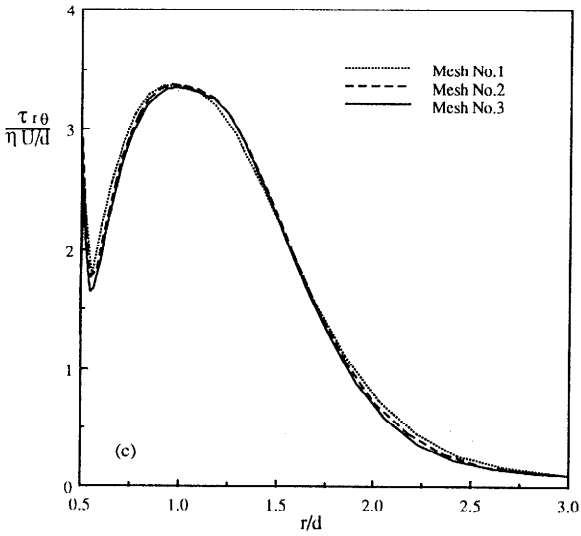


Fig. 4 (continued).

and the cylinder surface), when $\mathcal{R} = 4$, $E = 1$ and with the three meshes mentioned above. Figure 4 presents the values of the three extra stress components just above the cylinder ($\theta = \pi/2$) for the same parameters as in Fig. 3. We see that up to the value of Weissenberg number $W = 4$ which is an ordering parameter in the numerical simulation, the results obtained with these three meshes agree well. Meshes 2 and 3 resolve the stress boundary layer on the cylinder surface in the radial direction. However, for higher values of W , even mesh 3 is not fine enough as we shall see later. The computed drag coefficient and Nusselt number when $\mathcal{R} = 4$ and $E = 1$ for three meshes are listed in Table 1. For these three meshes, the Nusselt numbers for both $Pr = 1$ and $Pr = 10$ are almost identical; the difference in the drag coefficient is only about 1.1%.

TABLE 1			
The computed drag coefficient and Nusselt number when $\mathcal{R} = 4$ and $E = 1$ for three meshes			
	C_D	$Nu (Pr = 1)$	$Nu (Pr = 10)$
Mesh 1	8.94	1.19	2.03
Mesh 2	8.93	1.20	2.03
Mesh 3	8.83	1.20	2.03

5. Flow features

We first checked our code by running the program for the Newtonian case ($E = 0$) for which numerical and experimental results are available. Figure 5 plots the drag coefficient C_D and the Nusselt number Nu for a Newtonian fluid past a circular cylinder. The drag coefficient computed by the present method agrees perfectly with that obtained numerically by Sucker and Brauer [14], Takami and Keller [15] and Dennis and Chang [16]. The drag coefficient given in Delvaux and Crochet [11] is slightly higher than ours. We think that their small discrepancy may be due to a difference in the computation domain used. They restricted their computation to the flow around a cylinder inside a channel. In Fig. 5(b) we have compared the Nusselt numbers obtained by present computation with those given as experimental correlations by Davis [18] and Piret et al. [17] for two Prandtl numbers $Pr = 1$ and $Pr = 10$. Davis measured the heat loss from vertical wires in water and oils; his results were correlated by the equation

$$Nu = 0.91 Pr^{0.31} Re^{0.395} \quad \text{for } 0.1 < Re < 50. \quad (30)$$

Piret et al. [17] conducted similar experiments with horizontal wires in water, and found the relation

$$Nu = 0.965 Pr^{0.30} Re^{0.28} \quad \text{for } 0.08 < Re < 8. \quad (31)$$

For both $Pr = 1$ and $Pr = 10$ the agreement is quite good.

We next keep the flow fixed at certain Reynolds number and vary the elasticity number; thus we can look at the effect of the elasticity of the fluid on the flow. Figure 6 presents the streamlines in the neighborhood of the cylinder for flows at $Re = 10$ and E varying from 0 to 1.0. Figures 6(a) and 6(b) are almost identical. Starting from Fig. 6(c) with $M > 1$, we see an increasingly larger downstream shift of the streamlines; at the same time there is a relatively small upstream shift. The streamline pattern with viscoelastic fluids of large elasticity number differs significantly from that with Newtonian fluids. The large distortion of the streamlines creates a wide region near the cylinder where the velocity is very low, and thus affects the total drag on the cylinder and the heat transfer from the cylinder to the surrounding fluid as we will see later.

Figure 7 plots the isovorticity lines at $Re = 10$ and E varying from 0 to 1.0. Figure 7(a) is the familiar Newtonian case, where the isovorticity lines are swept downstream by the flow and the high vorticity region is at the front shoulder of the cylinder surface where the vorticity is being created. Figure 7(b) is basically the same as Fig. 7(a) except at the front of the cylinder where the isovorticity lines are closer together, signaling a sharper change of vorticity in this region. In Fig. 7(c), at a Mach number $M = 3.16$,

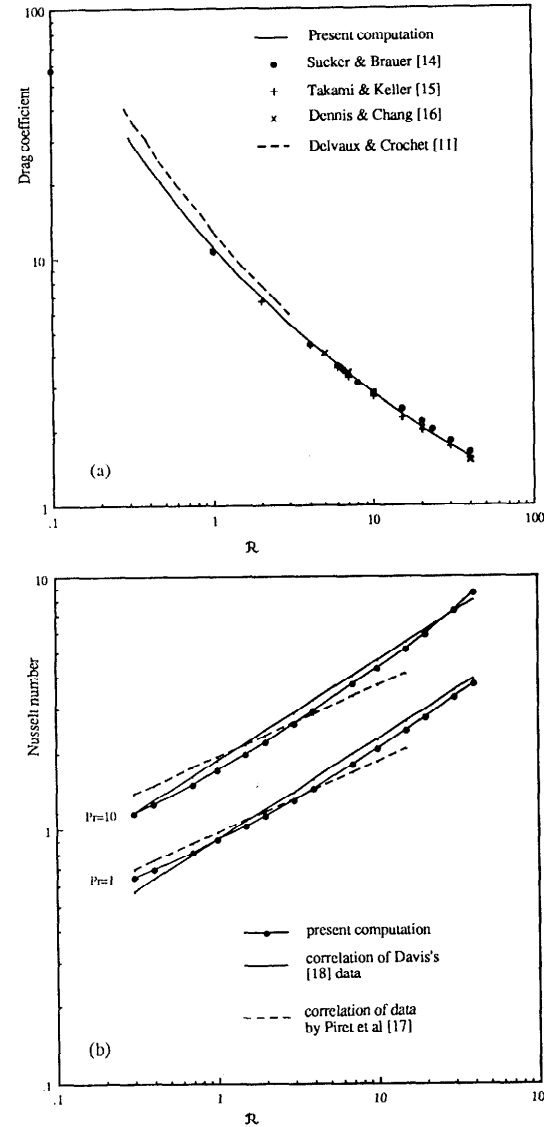


Fig. 5. Comparison of the drag coefficient C_D and the Nusselt number Nu for a Newtonian fluid past a circular cylinder. (a) Drag coefficient vs. Re . (b) Nusselt number vs. Re for $Pr = 1$ and $Pr = 10$.

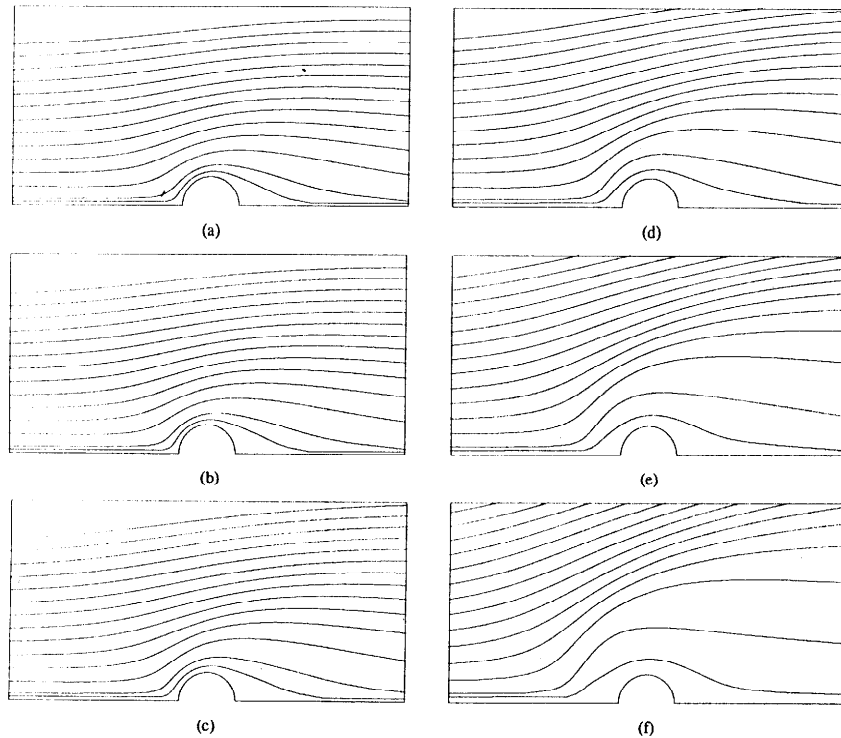


Fig. 6. Streamlines on the neighborhood of the cylinder for the flow of the same Reynolds number $\mathcal{R}=10$ and different elasticity numbers E . (a) $E=0$ ($M=0$). (b) $E=0.01$ ($M=1.0$). (c) $E=0.1$ ($M=3.16$). (d) $E=0.25$ ($M=5.0$). (e) $E=0.5$ ($M=7.07$). (f) $E=1.0$ ($M=10$). In the figures the values of the incoming streamlines, starting from the bottom, are 0.01, 0.05, 0.2, 0.4, 0.6, 0.8, 1.0, 1.2, 1.4, 1.6, 1.8, 2.0, 2.2 and 2.4.

we see that the isovorticity lines jam together at the front of the cylinder thus creating a vorticity shock, like a blunt body shock in gas dynamics. As the elasticity number increases, this shock still exists and moves slightly upstream. In Figs. 7(d)–7(f), the picture of the isovorticity lines for viscoelastic fluids with large relaxation time is drastically different from that of Newtonian fluids. As well as the high vorticity zone on the front shoulder of the cylinder surface which occurs already in the Newtonian case, there exists a second high vorticity region which starts to build up and shifts away from the cylinder surface as the elasticity number increases. We find that the maximum values of the vorticity in this second region are even higher than the maximum values of the vorticity on the cylinder surface, which suggests

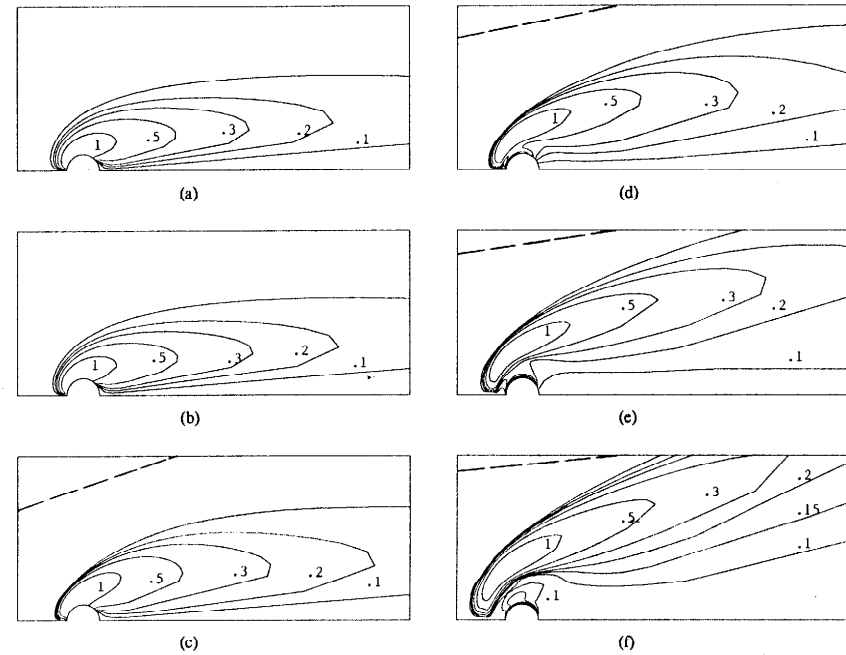


Fig. 7. Isovorticity lines for the flow of the same Reynolds number $\mathcal{R}=10$ and different elasticity numbers E . (a) $E=0$ ($M=0$). (b) $E=0.01$ ($M=1.0$). (c) $E=0.1$ ($M=3.16$). (d) $E=0.25$ ($M=5.0$). (e) $E=0.5$ ($M=7.07$). (f) $E=1.0$ ($M=10$). — — —, angle of the vorticity shocks predicted in the linearized theory.

generation of the vorticity away from the cylinder surface or behind the shock. We still do not understand the physical consequences of this build-up. The existence of this second high vorticity region away from the cylinder surface was also observed in the work of Delvaux and Crochet [11]; they found a local minimum and maximum in the vorticity plot along a path just above the cylinder ($\theta = \pi/2$). The broken lines in Fig. 7 indicate the angles, $\beta = \tan^{-1}(1/\sqrt{1-M^2})$, of vorticity shocks predicted in the linear theory in which the governing equations are linearized around the uniform income flow. Close to the cylinder, the vorticity shock is strong. The nonlinearity makes the shock curve around the cylinder. As E increases, the nonlinear region also increases owing to the large stagnant region around the cylinder. Since the linear theory is valid far away from the cylinder, the vorticity shock, if it exists, should eventually stretch with the angle predicted in the linear theory. However, because the shock is weak and the numerical space

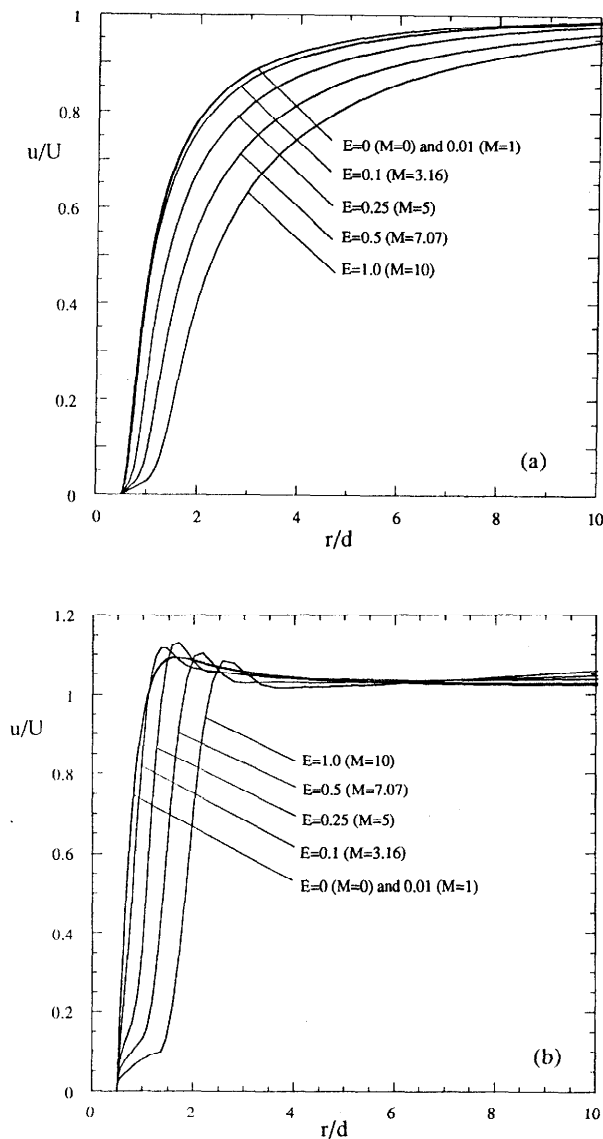


Fig. 8. Effects of viscoelasticity on the velocity profile. The results are obtained with $\mathcal{R} = 10$ and $E = 0, 0.01, 0.1, 0.25, 0.5, 1$. u is the velocity component in the direction of the free stream. (a) u vs. r along the path $\theta = 0$, ahead of the cylinder. (b) u vs. r along the path $\theta = \pi/2$, just above the cylinder.

discretization is usually coarse far away from the cylinder, it is very hard to capture this part of the shock numerically.

The velocity component u in the direction of the free stream is presented in Fig. 8 for $\mathcal{R} = 10$ and $E = 0, 0.01, 0.1, 0.25, 0.5, 1.0$. Figure 8(a) gives the profile of u ahead of the cylinder along the ray $\theta = 0$. Figure 8(b) gives the profile just above the cylinder along the ray $\theta = \pi/2$. It is clear that, for the flows of larger E , there is a region with small velocity close to the cylinder. This stagnant region grows with E . The diameter of this region has increased to about three times the cylinder diameter when $E = 1$ as seen in Fig. 8(b). Figure 8(a) also shows that there is a strong upstream influence for the viscoelastic flow with large E . In Fig. 8(b) we notice a velocity overshoot in the region above the cylinder. This overshoot exists for all cases with $M > 1$ and shifts away from the cylinder as E increases. The slope of the velocity profile in Fig. 8(b) is consistent with the vorticity (derivatives of the velocity) distribution above the cylinder, and indicates a second high vorticity region away from the cylinder surface.

Numerical integration is carried out for (28) on the cylinder surface to determine the drag force acting on the cylinder. The drag coefficient C_D is plotted in Fig. 9 as a function of \mathcal{R} for four values of $E = 0, 0.01, 0.1$ and 1 . The results for $E = 0, 0.01$ and 0.1 are obtained using mesh 2. For $E = 1$ the results using the other two meshes are also presented. We see that the mesh refinement has little influence on the drag coefficient for the range of parameters in our computation. In the figure we indicated the critical values of \mathcal{R} at which $M = 1$ for different E (for $E = 1$, $\mathcal{R} = 1$; $E = 0.1$, $\mathcal{R} = 3.16$ and $E = 0.01$, $\mathcal{R} = 0.1$). As \mathcal{R} increases beyond these critical values, the drag coefficient curves for viscoelastic flows begin to separate from the curve for Newtonian flow. The deviation is more evident for flows with large E . In the region of supercritical flow, $M > 1$, we see that the effect of the viscoelasticity is to increase the drag. This is consistent with the observation in the streamline plot (Fig. 6), which shows a nearly stagnant region around the cylinder. This stagnant region effectively increases the size of the cylinder, thus increases the total drag. We also noticed that the drag coefficient curves for $E = 1$ and $E = 0.1$ start to rise as \mathcal{R} becomes large enough. Delvaux and Crochet [11] found that a similar rise in C_D at large \mathcal{R} in their computation was due to numerical error. At first we thought that this rise might be caused by two numerical effects, the finite size of the mesh and our computation domain. We shall see in Fig. 13(a) that even mesh 3 is not fine enough to resolve the stress boundary layer on the cylinder surface. Therefore we designed a more refined mesh, mesh 4. This mesh has the same number of control volumes or grid points as mesh 3. The smallest control volume of mesh 4 in radial direction near the cylinder surface is of size $0.001d$, ten times smaller than that of mesh 3. The size of the control

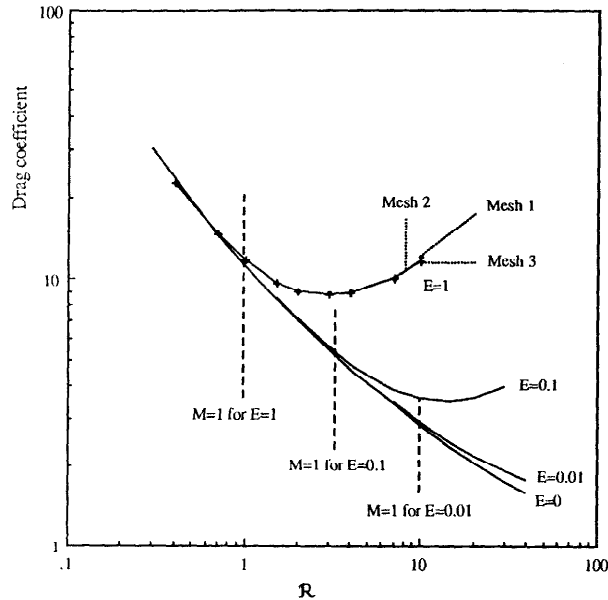


Fig. 9. Drag coefficient C_D vs. Reynolds number \mathcal{R} for elasticity numbers $E=0$ (Newtonian), 0.01, 0.1 and 1.0. —, results obtained using mesh 2; for $E=1$, the results obtained by the other two meshes are also plotted. — — —, values of the Reynolds number at which the viscoelastic Mach number $M=1$.

volumes in the r direction increases with a geometric ratio 1.17. The non-dimensional radius of the outer boundary is $r_\infty = 53.5$, or the size of the computational domain is 107 times the radius of the cylinder. Using this mesh, we checked our results for $E=1.0$, and found that the drag coefficient is almost the same as (or more precisely 1.4%, at maximum, less than) the results obtained using mesh 3 for large \mathcal{R} . Therefore we conclude that the rise of C_D at large \mathcal{R} is not due to a numerical effect. We re-examined the experimental data of James and Gupta [7], and found that their measured drag coefficient data showed a perceptible tendency to increase at high Reynolds number for some of the polymer solutions of high concentration.

The formula for the drag force acting on the cylinder (25) shows that the total drag can be separated into two parts, one part due to the pressure distribution around the cylinder and the other part due to the shear stress on the cylinder surface. These two contributions of the drag are plotted in Fig. 10. In the figure, the drag coefficients of a viscoelastic case $E=0.1$ are compared with those of the Newtonian case $E=0$. In the Newtonian case, when \mathcal{R} is small, the drag coefficients due to pressure and due to shear

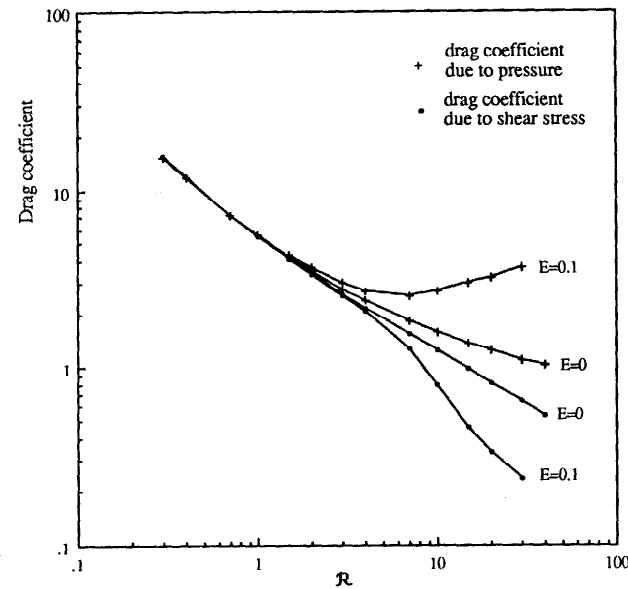


Fig. 10. Effect of the elasticity of the fluids on the drag due to pressure and the drag due to shear stress on the cylinder surface.

stress are equal, as is well known. The pressure drag coefficient increases with \mathcal{R} because of the wake generated behind the cylinder. This is especially true in the viscoelastic case, where the drag due to pressure can be much larger than the drag due to shear stress, as we see in the figure, since we have larger wakes in viscoelastic cases. The nearly stagnant region around the cylinder is also responsible for the reduction of the drag due to the shear stress in viscoelastic flow.

Figure 11 presents graphs of the Nusselt number Nu vs. \mathcal{R} for $E=0$, 0.01, 0.1 and 1 at $Pr=1$ and $Pr=10$. We checked the results for $E=1$ with three meshes. The results are almost identical. Again the values of \mathcal{R} at which $M=1$ are indicated in the figure with broken lines. For \mathcal{R} less than these critical values, the Nusselt number for viscoelastic flow is the same as that for Newtonian flow. For \mathcal{R} greater than the critical values, the Nusselt number deviates from the Newtonian path and tends to an asymptotic value which does not depend on \mathcal{R} . This deviation is more prominent for large E and Pr . We see that the effect of the viscoelasticity is to decrease the Nusselt number, or to reduce the heat transfer from the cylinder to the surrounding fluid. This can also be explained by the stagnant region which develops around the cylinder when the flow becomes supercritical ($M > 1$).

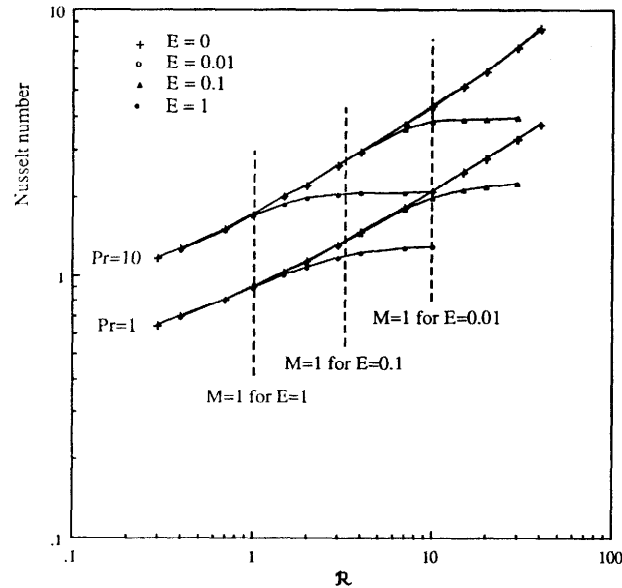


Fig. 11. Nusselt number Nu vs. Reynolds number Re for different elasticity numbers $E = 0$ (Newtonian), 0.01, 0.1, 1.0, and at Prandtl numbers $Pr = 1$ and 10. — — —, values of the Reynolds number at which the viscoelastic Mach number $M = 1$.

Finally, we shall examine the extra stress components. In Fig. 3, we show that there is a very large overshoot of the stress components τ_{rr} and $\tau_{\theta\theta}$ ahead of the cylinder. Along the ray $\theta = \pi/2$, the sharp variation of the extra stress components close to the cylinder surface indicate the existence of the stress boundary layer we have seen already in Fig. 4. Figure 12 shows the dimensionless $\tau_{\theta\theta}$ vs. r/d just above the cylinder at $\theta = \pi/2$ for $E = 1$ and different Re from 0.4 to 10. This figure also shows the development of the stress boundary layer as Re increases. The stress $\tau_{\theta\theta}$ is scaled with $2W$ in the figure since its value on the cylinder surface is $2W(\partial u_\theta/\partial r)^2$ as derived in the boundary condition (22). The results in Fig. 12(a) are obtained using mesh 3, and in Fig. 12(b) are obtained using the much refined mesh 4. We see that up to $Re = 10$ mesh 4 resolves the stress boundary layer well.

6. Comparison with experiments

We are going to compare our numerical results for the drag coefficient and Nusselt number with the results of experiments by James and Acosta [6]. In order to make the comparison we need to estimate the relaxation time

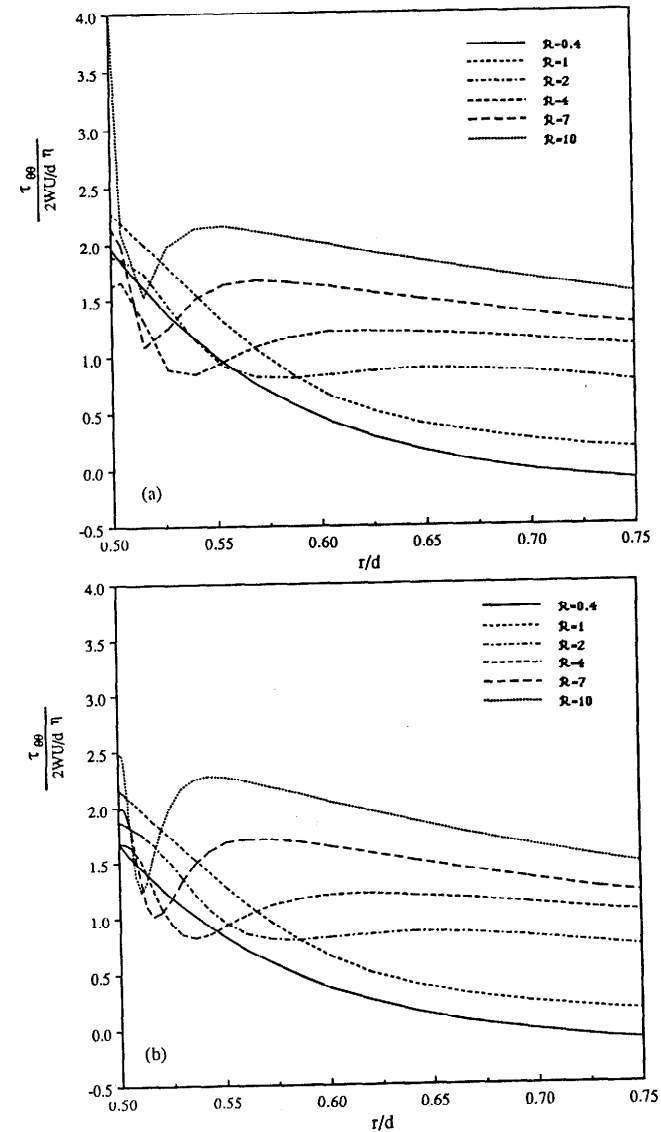


Fig. 12. Extra stress component $\tau_{\theta\theta}$ (scaled with $2W$) vs. r along the ray $\theta = \pi/2$ when $E = 1$ and $Re = 0.4, 1, 2, 4, 7, 10$. The graph shows the development of the stress boundary layer at the cylinder surface as Re increases. (a) Results obtained using mesh 3. (b) Results obtained using a much refined mesh, mesh 4. In (b) the stress boundary layer is well resolved up to $Re = 10$.

for the viscoelastic fluids used in the experiments. James and Acosta [6] derived an expression for a single relaxation time for dilute solutions based on molecular theory

$$\lambda = \frac{\eta_s [\eta]^2 M \phi}{RT} \quad (32)$$

where η_s is the viscosity of the solvent, $[\eta]$ the intrinsic viscosity, M the molecular weight, ϕ the concentration of solution, R the gas constant and T the temperature. This expression shows that λ is proportional both to the largest relaxation time of polymer molecules $\lambda_m = 6\eta_s[\eta]M/\pi^2RT$ and to the concentration ϕ , which appears quite reasonable on physical grounds. James and Gupta [7] generalized the derivation and showed significant influence of molecular weight distribution on the magnitude of relaxation time. They found expression (32) would underestimate the correct value of relaxation time by factors of $O(10)$ depending on the molecular weight distribution of polymers. Since the information about the molecular weight distribution for the polymers used in experiments is not known, we try to estimate the relaxation time using the shear wave speed, which can be measured experimentally.

We can measure shear wave speed of viscoelastic fluids using a wave speed meter [4]. From the measured value of wave speed c , we can estimate an effective relaxation time $\lambda_c = \eta/\rho c^2$. Thus we can evaluate the elasticity number for viscoelastic flows in experiments using the wave speed of polymer solutions:

$$E = \frac{\eta \lambda}{\rho d^2} = \left(\frac{\eta}{\rho c d} \right)^2 \quad (33)$$

The shear viscosity for dilute polymer solutions can be calculated using

$$\eta = \eta_s (1 + [\eta] \phi). \quad (34)$$

Inspired by the derivation of James and Acosta [6] and James and Gupta [7], we assume that for dilute polymer solutions relaxation time is proportional to concentration: $\lambda = A\phi$. A is a function of polymer properties such as those expressed in (32), and in general A depends on the molecular weight distribution of polymer, or it can even be a slowly varying function of ϕ . Based on this assumption we have the following relation between the wave speeds of dilute polymer solutions of two concentrations:

$$c_2 = c_1 \sqrt{\frac{\phi_1}{\phi_2}} \sqrt{\frac{1 + [\eta] \phi_2}{1 + [\eta] \phi_1}} \quad (35)$$

For extremely dilute solutions (35) simply reduces to

$$c = C\phi^{-1/2}, \quad (36)$$

where C is a function of polymer properties.

In the heat transfer experiments of James and Acosta [6], the Nusselt number for three Polyox solutions was found to deviate from the Newtonian data at a certain critical velocity. The analysis of Ultman and Denn [9] and Joseph [4] showed that this critical velocity was independent of the wire diameter, and more or less corresponded to the shear wave speed of the solution. In Fig. 13 we plot the critical velocity vs. concentration for three Polyox solutions and three diameters of wires used in the experiments. We see that the lines of $U_c = C\phi^{-1/2}$ correlate this critical velocity quite well. Ultman and Denn [9] (Fig. 3) also reproduced the variation of critical Reynolds number with concentration for the data of James and Acosta [6]. We find that straight line fitting in the log-log plot is better than their theoretical curve using Bueche's relaxation time.

Ambari et al. [19] measured the mass transfer from a small cylindrical wire in a dilute polymer solution using an electrochemical technique. They

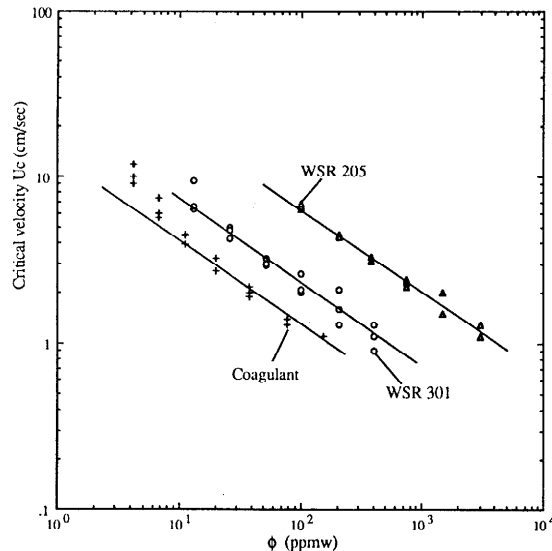


Fig. 13. Critical velocity at which the Nusselt number starts to deviate from the Newtonian data vs. concentration for three Polyox solutions (WSR-205, WSR-301, coagulant) and three cylindrical wires ($d = 0.001, 0.002, 0.006$ in). Data of James and Acosta [6]. —, correlations $U_c = C\phi^{-1/2}$.

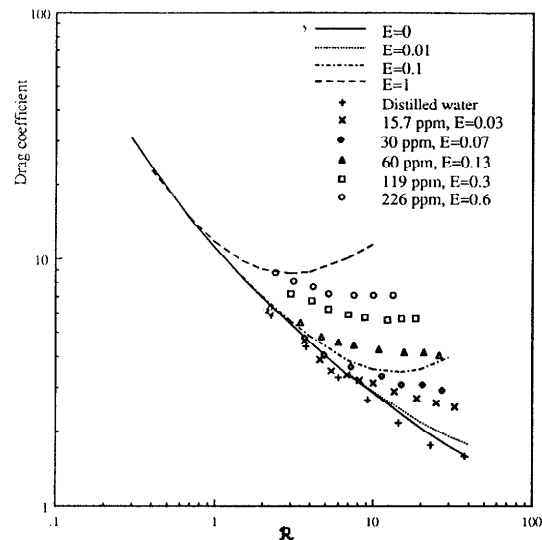


Fig. 14. Comparison of the drag coefficients obtained by the present computation (lines) with those measured in experiments of James and Acosta [6] (dots). The elasticity numbers for the experimental data are estimated using the shear wave speed as described.

found a large decrease of the mass transfer rate with respect to the Newtonian behavior, starting from a critical velocity. From their Fig. 3 we found that this critical velocity satisfies the same scaling law $U_c = C\phi^{-1/2}$ approximately.

For the drag coefficient, the experiments of James and Acosta [6] were carried out on a wire of diameter 0.005 in in solutions of Polyox WSR-301. The intrinsic viscosity of WSR-301 was $[\eta] = 9.6 \text{ g (100 ml)}^{-1}$ measured in the experiments. We reproduce the data for concentrations $\phi = 15.7, 30, 60, 119$ and 226 ppm by weight in Fig. 14. The shear wave speed for WSR-301 of concentration 50 ppm is about 2.48 cm s^{-1} , which is measured using a wave speed meter and listed in the tables of Joseph [4]. Using this wave speed, we can obtain the shear wave speeds for the other concentrations from relation (35). Thus we estimate elasticity numbers $E = 0.03$ for the set of data of 15.7 ppm , $E = 0.07$ for 30 ppm , $E = 0.13$ for 60 ppm , $E = 0.3$ for 119 ppm and $E = 0.6$ for 226 ppm as indicated in Fig. 14. These values are much larger, about 50 times larger, than the values estimated in James and Gupta [7]. As shown in Fig. 14 the agreement is fair.

In the Nusselt number (Fig. 15) we have reproduced the experimental data for distilled water and for Polyox WSR-301 of concentrations $26.2, 52.4, 102$ and 205 ppm in.

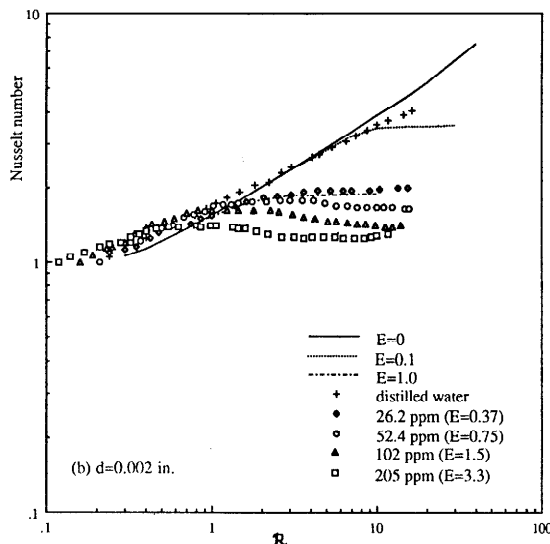
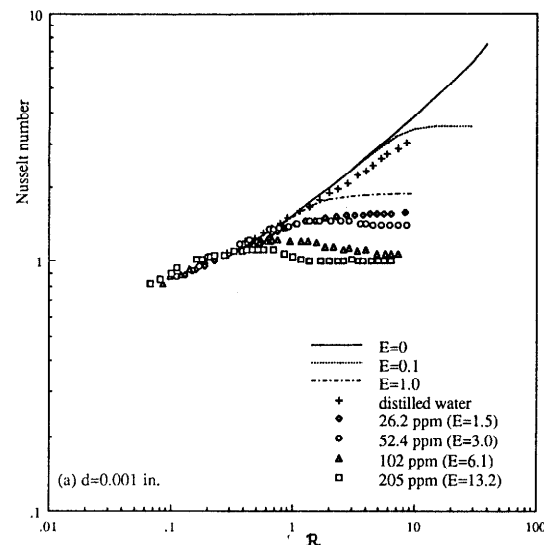


Fig. 15. Comparison of the Nusselt numbers obtained by the present computation (lines) with those measured in experiments of James and Acosta [6] (dots). (a) $d = 0.001 \text{ in.}$ (b) $d = 0.002 \text{ in.}$ (c) $d = 0.006 \text{ in.}$

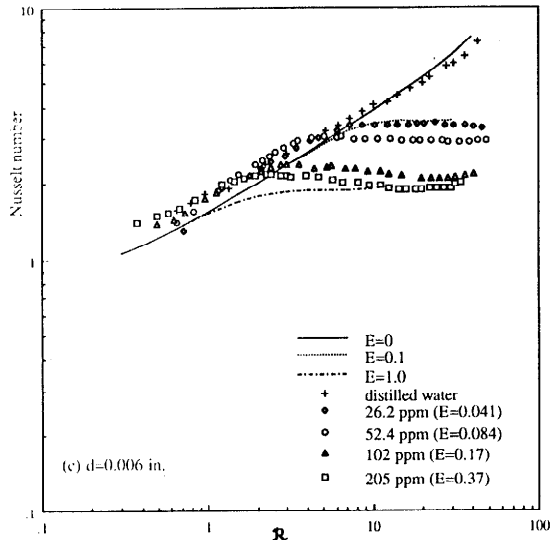


Fig. 15 (continued).

52.4, 119 and 227 ppm by weight with three wire diameters, $d = 0.006$ in, 0.002 in and 0.001 in. The elasticity numbers are similarly estimated and indicated in the figures. The experimental value of Pr is not known exactly; for distilled water at 20°C the Prandtl number is about 7. Thus the numerical results plotted in lines are obtained with $Pr = 7$. Qualitatively, the numerical results show the same tendency as the experimental results. The differences, we think, are due to many factors. Our estimation of the elasticity number is rough; as we see from (33), a 10% error in the shear wave speed causes 20% difference in E . The heat transfer experiments were carried out with a temperature difference varying from 9 to 33°C . This temperature difference changes the viscosity and the shear wave speed of the solution, and thus causes differences in the E . Also, our use of a Maxwell model with a single relaxation time to characterize the fluid will definitely induce some difference. However, at least, we can say that our numerical simulation appears to capture the principal features observed in experiments.

7. Conclusions

The algorithm SIMPLER works well for the flow of an upper-convected Maxwell fluid past a circular cylinder, and converges for relatively high

Weissenberg number. The numerical simulation captures the principal features observed in experiments.

For Re fixed as E increases, there is an increasingly larger downstream shift of the streamlines; at the same time there is a relatively small upstream shift. The distortion of the streamlines creates a wide region near the cylinder where the velocity is very low. This stagnant region grows with E .

In subcritical flow, $M < 1$, the drag on the cylinder for viscoelastic flow is the same as that for Newtonian flow. In supercritical flow, $M > 1$, viscoelasticity increases the drag. The drag due to pressure can be much larger than the drag due to shear stress for large Re .

In the region of $M < 1$, the Nusselt number for viscoelastic flow is the same as that for Newtonian flow. In the region of $M > 1$, the Nusselt number deviates from the Newtonian path and tends to an asymptotic value which does not depend on Re . This deviation is more prominent for large E and Pr .

In the region of $M > 1$, the isovorticity lines jam together at the front shoulder of the cylinder, creating a vorticity shock. When E is large, there exists a second high vorticity region away from the cylinder surface. The maximum values of the vorticity in this second region can be higher than the maximum values of the vorticity on the cylinder surface, which suggests generation of the vorticity away from the cylinder surface or behind the vorticity shock.

There is a very large overshoot of the stress components τ_{rr} and $\tau_{\theta\theta}$ ahead of the cylinder. There exists a stress boundary layer on the cylinder surface in the radial direction where the stresses $\tau_{\theta\theta}$ and $\tau_{r\theta}$ vary rapidly.

If we assume that the relaxation time $\lambda = A\phi$ is linear in ϕ for small ϕ , as in Einstein's viscosity formula, with A independent of ϕ , and use the empirical formula $\eta = \eta_w(1 + [\eta]\phi)$ where $[\eta]$ is the intrinsic viscosity and η_w the viscosity of water, then the ratio of wave speeds of two concentrations is

$$\frac{c_2}{c_1} = \sqrt{\frac{\phi_1}{\phi_2}} \sqrt{\frac{1 + [\eta]\phi_2}{1 + [\eta]\phi_1}}.$$

When ϕ is very small, in the drag reduction range, as in the experiment of James and Acosta [6] and James and Gupta [7], we find a scaling law for the wave speed:

$$c\phi^{1/2} = \text{constant}.$$

The measured values of the critical velocities U_c do appear to follow this scaling for all of the tests made by James and coworkers, lending credence to the idea that we are here seeing the effects of a change of type with $c = U_c$.

Acknowledgments

This work was started as a class project in the course Computation of Heat Transfer and Fluid Flow (ME8352) at University of Minnesota. The numerical solution of the problem in this paper is based on Patankar's method which was applied and implemented by one of us (H. Hu). Hu would like to thank Patankar for his stimulating lectures. We are also grateful to Marcel Crochet for alerting us to pitfalls, suggesting tests of mesh refinement and other helpful suggestions.

This work was supported by the Department of Energy, the National Science Foundation and the Army Research Office, Mathematics. Part of the computation was carried on a Cray-2 under a grant from the Minnesota Supercomputer Institute.

References

- 1 J.Y. Yoo, M. Ahrens and D.D. Joseph, Hyperbolicity and change of type in sink flow, *J. Fluid Mech.*, 153 (1985) 203–214.
- 2 D.D. Joseph and J.C. Saut, Change of type and loss of evolution in the flow of viscoelastic fluids, *J. Non-Newtonian Fluid Mech.*, 20 (1986) 117–141.
- 3 D.D. Joseph, J.E. Matta and K. Chen, Delayed die swell, *J. Non-Newtonian Fluid Mech.*, 24 (1987) 31–65.
- 4 D.D. Joseph, *Fluid Dynamics of Viscoelastic Liquids*, Springer, Berlin, 1990.
- 5 A.B. Metzner, E.A. Uebler and C.F.C.M. Fong, Converging flows of viscoelastic materials, *AIChE J.*, 15 (1969) 750–758.
- 6 D.F. James and A.J. Acosta, The laminar flow of dilute polymer solutions around circular cylinders, *J. Fluid Mech.*, 42 (1970) 269–288.
- 7 D.F. James and O.P. Gupta, Drag on circular cylinders in dilute polymer solutions, *Chem. Eng. Progr. Symp. Ser.*, 67 (111) (1971) 62–73.
- 8 A. Koniuta, P.M. Adler and J.M. Piau, Flow of dilute polymer solutions around circular cylinders, *J. Non-Newtonian Fluid Mech.*, 7 (1980) 101–106.
- 9 J.S. Utlman and M.M. Denn, Anomalous heat transfer and wave phenomenon in dilute polymer solutions, *Trans. Soc. Rheol.*, 14 (1970) 307–317.
- 10 M.J. Crochet and V. Delvaux, Numerical simulation of inertial viscoelastic flow with change of type, in: B. Keyfitz and M. Shearer (Eds.), *Nonlinear Evolution Equations that Change Type*, IMA Volumes in Mathematics and its Applications, Springer, Berlin, 1990.
- 11 V. Delvaux and M.J. Crochet, Numerical prediction of anomalous transport properties in viscoelastic flow, *J. Non-Newtonian Fluid Mech.*, 37 (1990) 297.
- 12 J.M. Marchal and M.J. Crochet, A new mixed finite element for calculating viscoelastic flow, *J. Non-Newtonian Fluid Mech.*, 26 (1987) 77–114.
- 13 S.V. Patankar, *Numerical Heat Transfer and Fluid Flow*, Hemisphere, New York, 1980.
- 14 D. Sucker and H. Brauer, *Fluiddynamik bei der angeströmten Zylindern*, *Wärme-Stoffübertrag.*, 8 (1975) 149.
- 15 H. Takami and H.B. Keller, Steady two-dimensional viscous flow of an incompressible fluid past a circular cylinder, *Phys. Fluids*, 12 (Suppl. II) (1969) 51.
- 16 S.C.R. Dennis and G.Z. Chang, Numerical solutions for steady flow past a circular cylinder at Reynolds number up to 100, *J. Fluid Mech.*, 42 (1970) 471.
- 17 E.L. Piret, W. James and M. Stacy, Heat transmission from fine wires to water, low velocity data and correlation, *Ind. Eng. Chem.*, 39 (1947) 1098–1103.
- 18 A.H. Davis, Convective cooling of wires in stream of viscous liquids, *Philos. Mag.*, 47 (1924) 1057–1092.
- 19 A. Ambari, C. Delslouis and B. Tribollet, Coil–stretch transition of macromolecules in laminar flow around a small cylinder, *Chem. Eng. Commun.*, 29 (1984) 63–78.